The Astrophysical Journal, 974:222 (11pp), 2024 October 20 https://doi.org/10.3847/1538-4357/ad62fc
© 2024. The Author(s). Published by the American Astronomical Society.
OPEN ACCESS

Simulating Brown Dwarf Observations for Various Mass Functions, Birthrates, and Low-mass Cutoffs

Yadukrishna Raghu[1,2,3], J. Davy Kirkpatrick[1,3], Federico Marocco[1,3], Christopher R. Gelino[4], Daniella C. Bardalez Gagliuffi[3,5], Jacqueline K. Faherty[3,5], Steven D. Schurr[1], Adam C. Schneider[3,6], Aaron M. Meisner[3,7], Marc J. Kuchner[3,8], Hunter Brooks[3,9], and Jake Grigorian[10,11]
The Backyard Worlds: Planet 9 Collaboration
[1] IPAC, Mail Code 100-22, California Institute of Technology, 1200 E. California Blvd., Pasadena, CA 91125, USA; yadukrishnaraghu01@gmail.com
[2] Washington High School, 38442 Fremont Blvd., Fremont, CA 94536, USA
[3] Backyard Worlds: Planet 9
[4] NASA Exoplanet Science Institute, Mail Code 100-22, California Institute of Technology, 770 S. Wilson Ave., Pasadena, CA 91125, USA
[5] Department of Astrophysics, American Museum of Natural History, Central Park West at 79th St., New York, NY 10024, USA
[6] United States Naval Observatory, Flagstaff Station, 10391 W. Naval Observatory Rd., Flagstaff, AZ 86005, USA
[7] NSF's National Optical-Infrared Astronomy Research Laboratory, 950 N. Cherry Ave., Tucson, AZ 85719, USA
[8] NASA Goddard Space Flight Center, Exoplanets and Stellar Astrophysics Laboratory, Code 667, Greenbelt, MD 20771, USA
[9] Department of Astronomy and Planetary Science, Northern Arizona University, Flagstaff, AZ 86011, USA
[10] University of Southern California, University Park Campus, Los Angeles, CA 90089, USA
[11] Saint Francis High School, 200 Foothill Blvd., La Cañada, CA 91011, USA
Received 2023 September 20; revised 2024 May 3; accepted 2024 May 5; published 2024 October 14

Abstract

After decades of brown dwarf discovery and follow-up, we can now infer the functional form of the mass distribution within 20 pc, which serves as a constraint on star formation theory at the lowest masses. Unlike objects on the main sequence that have a clear luminosity-to-mass correlation, brown dwarfs lack a correlation between an observable parameter (luminosity, spectral type, or color) and mass. A measurement of the brown dwarf mass function must therefore be procured through proxy measurements and theoretical models. We utilize various assumed forms of the mass function, together with a variety of birthrate functions, low-mass cutoffs, and theoretical evolutionary models, to build predicted forms of the effective temperature distribution. We then determine the best fit of the observed effective temperature distribution to these predictions, which in turn reveals the most likely mass function. We find that a simple power law ($dN/dM \propto M^{-\alpha}$) with $\alpha \approx 0.5$ is optimal. Additionally, we conclude that the low-mass cutoff for star formation is $\lesssim 0.005\,M_{\odot}$. We corroborate the findings of Burgasser, which state that the birthrate has a far lesser impact than the mass function on the form of the temperature distribution, but we note that our alternate birthrates tend to favor slightly smaller values of α than the constant birthrate. Our code for simulating these distributions is publicly available. As another use case for this code, we present findings on the width and location of the subdwarf temperature gap by simulating distributions of very old (8–10 Gyr) brown dwarfs.

Unified Astronomy Thesaurus concepts: Stellar mass functions (1612); Initial mass function (796); Brown dwarfs (185); Star formation (1569); Solar neighborhood (1509)

1. Introduction

First detected in 1995 (Nakajima et al. 1995; Oppenheimer et al. 1995), brown dwarfs, defined to be objects below the hydrogen 1 fusing limit of $\sim 0.075\,M_{\odot}$ (Hayashi & Nakano 1963; Kumar 1963), bridge the mass gap between hydrogen-fusing stars and exoplanets. Despite the substantial advancements of understanding that the field of brown dwarf astronomy has experienced in the past two decades through infrared missions such as the National Aeronautics and Space Administration's (NASA) Wide-field Infrared Survey Explorer (WISE; Wright et al. 2010) and NASA's Spitzer Space Telescope (Werner et al. 2004), there is still an abundance of open questions regarding many aspects of brown dwarfs. Examples are the exact formation mechanisms that prevail in different mass regimes, as well as the low-mass cutoff of this formation process. Answering these questions and improving the theory necessitates additional brown dwarf observational data, be they spectroscopic or photometric. However, observing brown dwarfs is an ordeal in itself, with some known examples as faint as ~28 mag at 1.15 μm (James Webb Space Telescope F115W filter) and at an estimated distance greater than 570 pc (Nonino et al. 2023). However, the distance itself is not necessarily the defining factor in a brown dwarf's faintness, since exceedingly close brown dwarfs have also been observed to be especially faint. The leading example is WISE J085510.83−071442.5, which is confidently estimated to have a $J_{\rm MKO} > 24.0$ mag (Faherty et al. 2014) at ~2.3 pc (Kirkpatrick et al. 2021). Compounding this dilemma is the considerable challenge of reliably measuring the physical properties of the object, such as mass, age, and temperature. Those familiar with the methods of stellar astronomy will recall that the masses of main-sequence stars can be derived with little uncertainty using only a few common observables, such as color, absolute magnitude, or spectral type. However, brown dwarfs do not possess such simple relations between physically observable quantities and mass. A brown dwarf of a certain temperature or spectral type may have a range of possible

Original content from this work may be used under the terms of the Creative Commons Attribution 4.0 licence. Any further distribution of this work must maintain attribution to the author(s) and the title of the work, journal citation and DOI.

masses. Such a coupling of parameters is a consequence of cooling over astronomical timescales, as brown dwarfs cool continually throughout their lifetimes. This means that a massive old brown dwarf that has cooled can have a similar temperature to a lower-mass young brown dwarf.

Despite this observational barrier, techniques have been formulated to directly derive the mass of a brown dwarf, yet they can often only be employed in rare, opportune cases.

For resolvable brown dwarf binary systems, one may leverage the orbital dynamics of the system and then solve for the mass of the brown dwarf. To measure the mass of our desired object, M_2, we need the semimajor axes of both orbits, a_1 and a_2, as well as the orbital period P, inclination i, and gravitational constant G (Carroll & Ostlie 1996):

$$M_2 = \frac{4\pi^2(a_1 + a_2)^3}{GP^2\left(\frac{a_2}{a_1} + 1\right)\cos^3 i}. \quad (1)$$

Alternatively, there is microlensing, in which we observe a brown dwarf passing between a background light source and the observer. Since the mass of the transiting brown dwarf affects the path of the light emitted by the background star due to gravitational lensing, one can determine the mass of the lens by measuring the displacement and amplification of the light emitted by the background object (Dominik & Sahu 2000; Cushing et al. 2014).

Nevertheless, occasions in which we are able to apply these methods are exceptionally rare. The current methods of direct observation would provide only a handful of directly observed or inferred masses in any volume-limited sample. One notable exception to this are brown dwarf constituents of a young star formation region or moving group, for which a robust age can be assumed for all objects. Drawbacks in this case are a higher reliance on evolutionary models at young ages, interstellar reddening (since these clusters are more distant than the local sample and are often still enshrouded in dust), and difficulties in resolving close multiple systems and assuring completeness of the brown dwarf sample.

Since we find ourselves at an impasse when pursuing direct paths of constructing and validating the mass distributions for brown dwarfs, we instead choose to use the temperature of brown dwarfs as a proxy measurement to indirectly constrain the brown dwarf mass function. Although accessing temperature data is not as simple for brown dwarfs as for main-sequence stars, it is a far more accessible measurement than direct brown dwarf mass measurements. We compare our predicted distributions with the observational distribution of brown dwarf temperatures (e.g., Kirkpatrick et al. 2019). In our study, we construct theoretical temperature distributions with the inverse transform method, assuming theoretical mass and age distributions that have found success in previous literature (Johnson et al. 2021; Kirkpatrick et al. 2019, 2021).

Then, we make use of a variety of brown dwarf evolutionary models, all with somewhat different assumed internal physics, to calculate the temperature of each object. Combining these calculated temperatures across a simulated population allows us to build its temperature distribution. From here, the problem becomes one of optimization, as we seek to obtain the particular set of parameters (functional form of the mass function, birthrate, low-mass cutoff, and evolutionary model suite) that results in a temperature distribution whose shape most accurately fits the observed distribution. Our extensive sampling of the permutations of parameters constrains the functional form of the brown dwarf mass function.

In Section 2, we present our chosen mass functions, which we need for the implementation of the inverse transform methodology. We also discuss the topic of the low-mass cutoff for brown dwarfs. In Section 3, we explore different proposed age distributions, and Section 4 examines the evolutionary models we use as well as their physical implications. Section 5 combines the tools developed in the three preceding sections to create our simulated brown dwarf populations and their temperature distributions. Section 6 contains a comparison of our simulated stellar populations to our empirical data, as well as an analysis of the impact of certain parameters on the derived temperature distribution. In Section 7, we provide our concluding remarks and possible avenues of future research.

2. Mass Distributions

Past studies of the functional form of the stellar mass distribution are replete with power-law formalisms. Power laws have been found to represent the functional forms seen in the 0.3–10 $M_\odot$ (Salpeter 1955) and 0.1–63 $M_\odot$ (Miller & Scalo 1979) regimes. In addition to the two power-law mass functions needed to describe (higher-mass) stars, there may be a third, separate power-law form needed for the (lower-mass) brown dwarf regime (Kirkpatrick et al. 2021), along with a fourth in the M dwarf regime (Kirkpatrick et al. 2023). The youthfulness of the field of brown dwarf science combined with a lack of ample data sets has meant that many functional forms have been theorized. Some examples of these are the lognormal (Chabrier 2001, 2003a, 2003b; Chabrier & Lenoble 2023) and the bipartite power law from Kroupa et al. (2013, their Equation (55)). The physics of the brown dwarf formation mechanism(s) will ultimately determine the way that the mass in the natal cloud is distributed among the birthed objects. Each birth mechanism results in a different mass distribution for brown dwarfs; for example, a power law arises from stellar birth physics that is independent of the size of the natal cloud (Kirkpatrick et al. 2021). On the other hand, the lognormal implies a set of multiplicative birth parameters (Kapteyn 1903).

As previous investigations of the substellar mass function have found simple power laws to be the favored functional form (Kirkpatrick et al. 2019, 2021), we also choose to adopt a simple power law as our proposed mass distribution, or probability distribution function (PDF), of brown dwarfs. The functional form of this simple power law is written in Equation (2) with parameter α, constant of normalization C_N, and input mass $\mathcal{M}$:

$$\mathrm{PDF}(\mathcal{M}) = C_N \mathcal{M}^{-\alpha}. \quad (2)$$

2.1. Low-mass Cutoff

A crucial parameter of brown dwarf formation is the value of the low-mass cutoff, which has been shown to be no higher than $\sim$10 M_{Jup} (Kirkpatrick et al. 2021). Objects such as WISE J085510.83−071442.5, which is estimated to a have a mass between 1.5 M_{Jup} and 8 M_{Jup}, depending on its age (Leggett et al. 2017), along with objects identified in young moving groups (see below), almost certainly push this limit lower, as seen by derived low-mass cutoffs of $\sim$4 M_{Jup} in Bate & Bonnell (2005).

The lowest mass at which brown dwarfs form is a fundamental property of star formation at the very edge of our theoretical understanding of brown dwarfs. Notably, a lower-mass cutoff not only extends the mass range in which brown dwarfs may form but also shifts the mode of the distribution to lower masses. These faint objects that would populate the low-mass end of the mass function are predominantly late T and Y dwarfs, as seen in Figure 6 of Burgasser (2004). The observed space density in temperature bins below 750 K has the greatest deciding influence on the value of the low-mass cutoff, as lower-mass cutoffs will more heavily populate objects at the lowest temperatures. Thus, data at these coolest temperatures will be most influential in determining the low-mass cutoff.

Due to the faint nature of late T and Y dwarfs, it is difficult to complete a volume-limited sample with sufficient statistics to provide a robust space density measurement. Since the lowest-temperature bins are of paramount importance for the evaluation of the low-mass cutoff, we need additional discoveries of faint, cold Y dwarfs in order to further constrain the value of the low-mass cutoff.

For this study, we choose 0.01 $M_\odot$, 0.005 $M_\odot$, and 0.001 $M_\odot$ as the low-mass cutoffs within our framework, as was done in Kirkpatrick et al. (2021). These values produce populations that include low-mass brown dwarfs that either straddle or are below the deuterium-burning limit (~13 $M_{\rm Jup}$; Spiegel et al. 2011). There are precedents for such brown dwarfs. Take, for example, the low-mass brown dwarfs SIMP J013656.5+093347.3 and 2MASSW J2244316+204343. SIMP J013656.5+093347.3 is a young early T dwarf with an estimated mass of 12.7 ± 1.0 $M_{\rm Jup}$, derived using its moving group association and evolutionary models (Saumon & Marley 2008), and a trigonometric distance of 6.139 ± 0.037 pc (Gagné et al. 2017). 2MASSW J2244316 +204343 is a mid-L dwarf with a mass of 10.46 ± 1.49 $M_{\rm Jup}$ (Faherty et al. 2016), also derived from evolutionary models, and a kinematic distance of 18.5 ± 1.2 pc (Liu et al. 2016). However, both objects are close to the solar system and therefore less of a challenge for the current instrumentation to observe, unlike further, fainter brown dwarfs.

2.2. Deriving the Inverse Cumulative Distribution Function

Integrating Equation (2), supposing $\alpha \neq 1$, to find our cumulative distribution function (CDF), we get the following expression, where M is the mass parameter. Our CDF, once normalized and inverted, will serve as a key component of the inverse transform method that we utilize. Here, m_2 is the high-mass cutoff, defined to be 0.1 $M_\odot$, and we vary m_1 between 0.01 $M_\odot$, 0.005 $M_\odot$, and 0.001 $M_\odot$:

$$\mathrm{CDF}(M) = C_N \int_{m_1}^{M} \mathcal{M}^{-\alpha} d\mathcal{M} = \frac{C_N(M^{1-\alpha} - {m_1}^{1-\alpha})}{1-\alpha}. \quad (3)$$

In order to derive our constant of normalization, C_N, we need our CDF to evaluate to 1 given the higher-mass limit. Solving for the constant, we find the following:

$$\mathrm{CDF}(M = m2) = 1 = \frac{C_N({m_2}^{1-\alpha} - {m_1}^{1-\alpha})}{(1-\alpha)}, \quad (4)$$

$$C_N = \frac{1-\alpha}{({m_2}^{1-\alpha} - {m_1}^{1-\alpha})}. \quad (5)$$

Similarly, when $\alpha = 1$ in Equation (2), the constant of normalization is the following:

$$C_N = \frac{1}{\ln(m_2) - \ln(m_1)}. \quad (6)$$

Once inverted and with the value of C_N inserted, the equation for CDF^{-1} becomes the following (Kirkpatrick et al. 2019):

$$\mathrm{CDF}^{-1}(x) = \begin{cases} [x({m_2}^{1-\alpha} - {m_1}^{1-\alpha}) + {m_1}^{1-\alpha}]^{\frac{1}{1-\alpha}}, & \text{for } \alpha \neq 1 \\ e^{x[\ln(m_2) - \ln(m_1)] + \ln(m1)}, & \text{for } \alpha = 1. \end{cases}$$

Here, $x \in \mathcal{U}_{[0,1]}$, meaning x is randomly sampled from the uniform distribution between 0 and 1. Histograms of the CDF^{-1} sampled 10^6 times per low-mass cutoff threshold with various α values are shown in Figure 1.

3. Age Distributions

We employ three different potential birthrate distributions in our main analysis (Figure 2). In Sections 3.1–3.3, we state the functional form of each birth time distribution and provide a few remarks on their underlying physics. Our study considers the last 10 Gyr out of the 15 Gyr of Galactic disk stellar formation activity modeled in Johnson et al. (2021), from which come our inside-out and late-burst birthrates. Since the evolutionary models we use (see Section 4) depend on age as opposed to time, we convert each time distribution into an age distribution by the following coordinate transformation, in which $\mathcal{A}$ and $\mathcal{T}$ are the age and time parameters, respectively, all in units of Gyr:

$$\mathrm{PDF}(\mathcal{A}) = \mathrm{PDF}(15 - \mathcal{T}). \quad (7)$$

We calculate the normalized CDF^{-1} of each of our proposed age distributions for later use in Section 4. Detailed studies of stellar formation processes and history can be found in Johnson et al. (2021). However, for our purposes, we use age distributions only as an auxiliary measurement in our study of mass distributions, especially since ultimately, the age distribution of a brown dwarf population has an undersized influence on its temperature distribution (Burgasser 2004).

3.1. Constant Distribution

The constant birthrate function is a common starting point by virtue of its inherent simplicity. A constant distribution implies that the galaxy's star formation processes have been consistently efficient and have had sufficient star-forming material from nascence to the present day. We adopt the following functional form for the constant distribution, in which $C_\mathcal{T}$ is the eponymous constant of star formation:

$$\mathrm{PDF}(\mathcal{T}) \propto C_\mathcal{T}. \quad (8)$$

The value of $C_\mathcal{T}$ is not of much significance in our study, as we ultimately normalize our CDF.

Given that the constant age distribution is, as its name implies, constant, it does not depend on any time parameter $\mathcal{T}$. Therefore, in order to convert it from an age distribution, we simply change $C_\mathcal{T}$ to $C_\mathcal{A}$ to indicate the change from a constant of time to a constant of age, instead of executing the coordinate

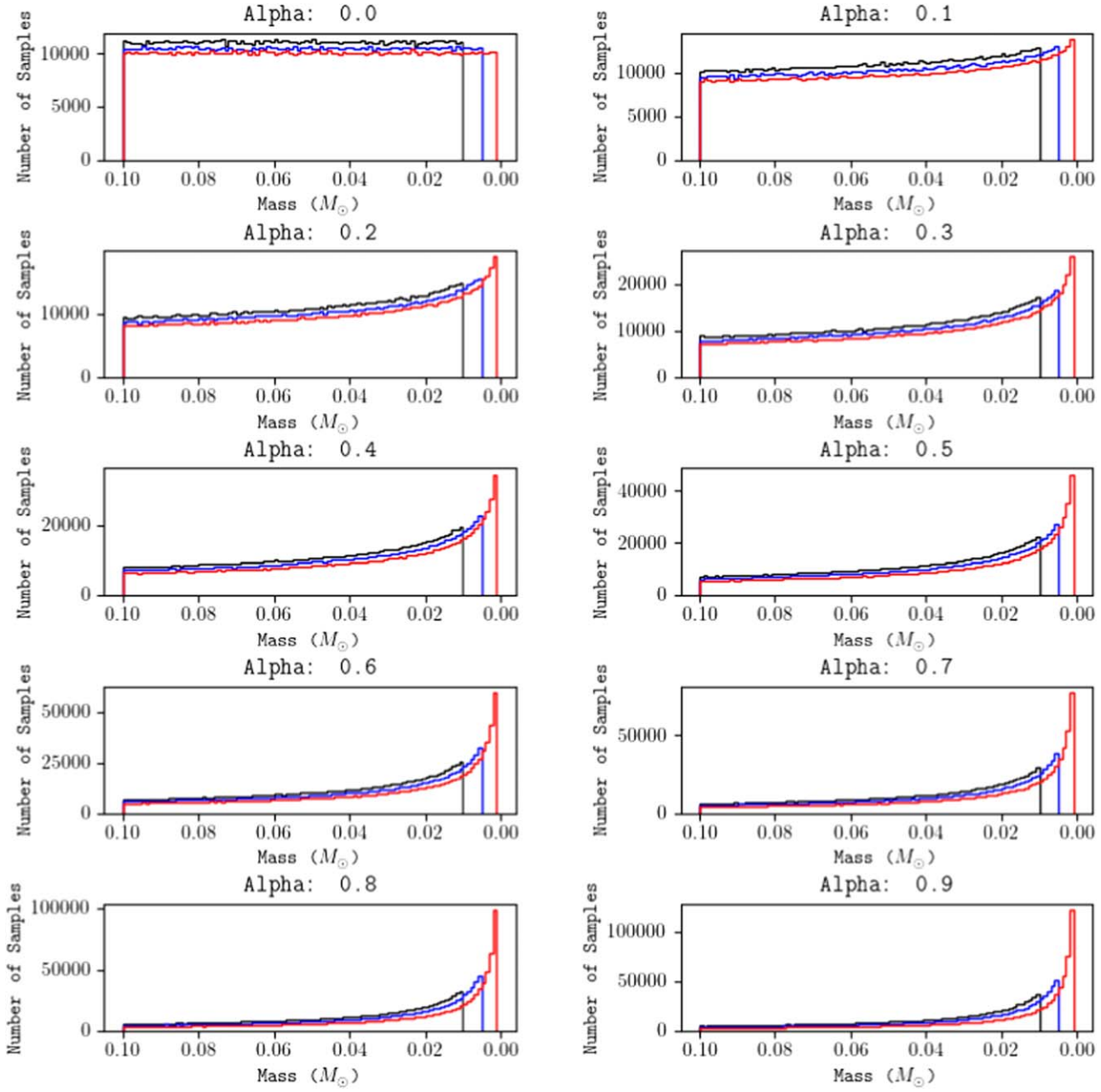

Figure 1. Sampled histograms of the CDF^{-1}, with the α value ranging from 0 to 0.9, in increments of 0.1. Red is the 0.001 $M_\odot$ low-mass cutoff, blue is the 0.005 $M_\odot$ low-mass cutoff, and black is the 0.01 $M_\odot$ low-mass cutoff.

transformation outlined in Equation (7):

$$\mathrm{PDF}_C(\mathcal{A}) \propto C_{\mathcal{A}}. \tag{9}$$

The CDF^{-1} for our constant distribution can be attained in a manner similar to Section 2.2:

$$\mathrm{CDF}_C^{-1}(x) = x(a_2 - a_1) + a_1. \tag{10}$$

We choose to leave CDF_C^{-1} in terms of a_1 to a_2, the minimum and maximum ages in Gyr, respectively, as our study explores more than one age range; see the Appendix.

3.2. Inside-out Distribution

The inside-out age distribution represents a sample population where star formation initiates within the central regions of the galaxy and propagates outward with time (Bird et al. 2013). The functional form of the distribution is the following (Johnson et al. 2021):

$$\mathrm{PDF}(\mathcal{T}) \propto (e^{\frac{-t}{15}}(1 - e^{\frac{-t}{2}})). \tag{11}$$

We choose to linearly approximate this time distribution using Equation (12), since inverting the CDF of Equation (11) requires the use of the computationally expensive error function $\left(\mathrm{erf}(x) = \frac{2}{\sqrt{\pi}} \int_0^x e^{-t^2} dt\right)$. Moreover, the original functional form is already sufficiently linear between our age bounds of 0 and 10 Gyr such that our approximation retains much of the original shape of the function:

$$\mathrm{PDF}_{IO}(\mathcal{T}) \propto (-0.03\mathcal{T} + 0.81). \tag{12}$$

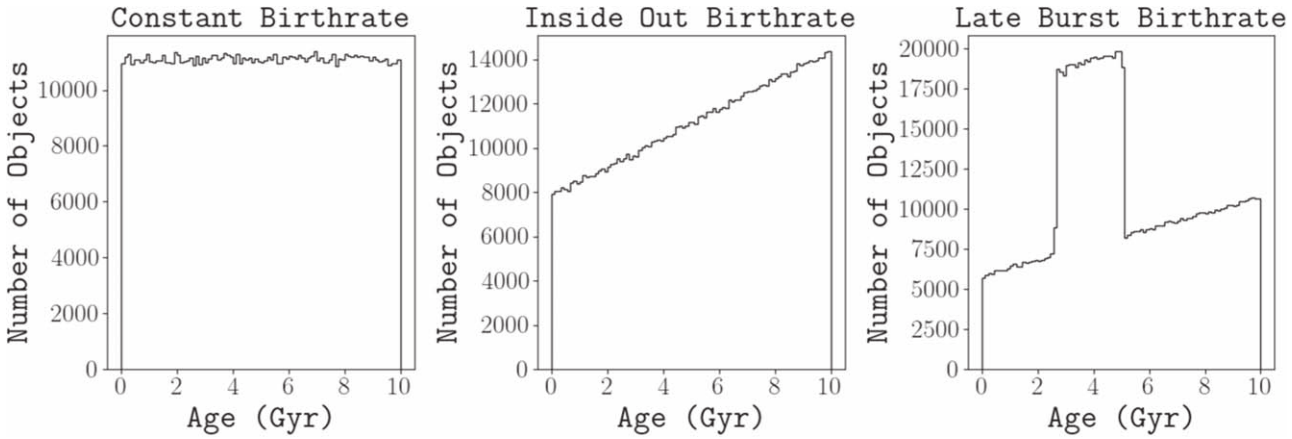

Figure 2. Histograms with 10^6 samples of the CDF^{-1} for each of our three different birthrates. Note that these graphs display the birthrates after having switched from the time domain to the age domain.

By using Equation (7) to convert this time distribution to an age distribution, we arrive at the following functional forms:

$$\mathrm{PDF}_{IO}(\mathcal{A}) \propto (0.03\mathcal{A} + 0.36). \tag{13}$$

Integrating and normalizing this PDF yields the following CDF for the inside-out birthrate:

$$\mathrm{CDF}_{IO}(A) = \frac{1}{5.1}\left(\frac{0.03}{2}A^2 + 0.36A\right) = x. \tag{14}$$

We solve for A as we have done previously to derive the inverse form of the CDF. The negative branch of the solution is disregarded, as a negative age is physically inconceivable:

$$\mathrm{CDF}_{IO}^{-1}(x) = -12 + \sqrt{(144 + 340x)}. \tag{15}$$

3.3. Late-burst Distribution

Galactic star formation need not have followed a constant rate or even one that varies linearly like the inside-out distribution. In the past 10 Gyr, it is possible that periods of the star formation history of our Galaxy have been more intense than others, with otherwise linear reduction of the birthrate, as seen in the inside-out distribution. This manifests itself as bursts of increased star formation, possibly due to gravitational perturbances from the Sagittarius dwarf galaxy (Ruiz-Lara et al. 2020) or from an earlier galactic merger incident inducing a starburst in our Galaxy (Helmi 2020).

The late-burst model accounts for such a period of starburst with a spike in the disk's total birthrate between the ages of 2.65 and 5.10 Gyr. Equation (16) displays the mathematical expression for the late-burst model. For ease of inversion, we approximate the late-burst model as Equation (17), defined in terms of the two previous birthrates, PDF_C and PDF_{IO}:

$$\mathrm{PDF}(\mathcal{T}) \propto (e^{\frac{-\mathcal{T}}{15}}(1 - e^{\frac{\mathcal{T}}{2}})(1 + 1.5e^{-\frac{(\mathcal{T}-11.2)^2}{2}}), \tag{16}$$

$$\mathrm{PDF}_{\mathrm{LB}}(A) \propto \begin{cases} \mathrm{PDF}_{IO}, & \text{for } 0 - 10 \text{ Gyr} \\ \mathrm{PDF}_{IO} + \mathrm{PDF}_C, & \text{for } 2.65 - 5.10 \text{ Gyr} \end{cases}. \tag{17}$$

In order to extract a meaningful CDF^{-1} from this, we integrate each piece of the late-burst model and allocate samples to preserve the ratio between the two pieces. Thus, the $\mathrm{CDF}_{\mathrm{LB}}^{-1}$ is a mixture of CDF_{IO}^{-1} and CDF_C^{-1}, whose individual sample sizes depend on the area under each individual PDF.

4. Evolutionary Models

Theoretical models predicting the evolution of brown dwarfs have been formulated, each one presupposing different physics of brown dwarf cooling. In our study, we consider the three following evolutionary models: Sonora (Marley et al. 2021), Saumon & Marley 2008 (Saumon & Marley 2008), and Phillips (Phillips et al. 2020). Figure 3 shows the grid of cross sections of the sampled parameter space in mass, age, and temperature covered by each of the evolutionary models.

The particular features of each model relevant to our investigation are delineated below.

1. Saumon & Marley (2008) is our only model that incorporates the effects of dust during the L–T transition, seen as atmospheric cloud cover at the spectral type transition (Burrows et al. 2006). This model does not include objects that are either massive and young (masses $\geqslant 0.06\,M_\odot$ and ages $\leqslant 1$ Gyr) or light and old (masses $\leqslant 0.01\,M_\odot$ and ages $\geqslant 1$ Gyr), as seen by the lack of reference points in the bottom right and top left corners of the top left subplot in Figure 3.
2. The Marley et al. (2021) model features updated chemistry (see their Section 2) but notably lacks the earlier assumption of dust and cloud formation during the L–T transition. This model is better sampled than its predecessor for old, light stars, yet it does not extend to objects that are massive and young (mass $\geqslant 0.06\,M_\odot$ and age $\leqslant 1$ Gyr).
3. The Phillips (Phillips et al. 2020) model set offers three evolutionary grids, one using equilibrium chemistry and two using nonequilibrium with differing vertical mixing strengths, of which we choose to use the evolutionary model with weak mixing. This evolutionary model also does not account for L–T transition dust and cloud formation, although it is far more thoroughly sampled in the mass–age space than both of the other evolutionary models we consider.

5. Methods

Our primary objective is as follows: determining the best-fit functional form of the substellar mass distribution using the volume-complete sample of brown dwarfs within 20 pc of the Sun.

We outline how we create populations with masses and ages consistent with their assumed mass and age distribution

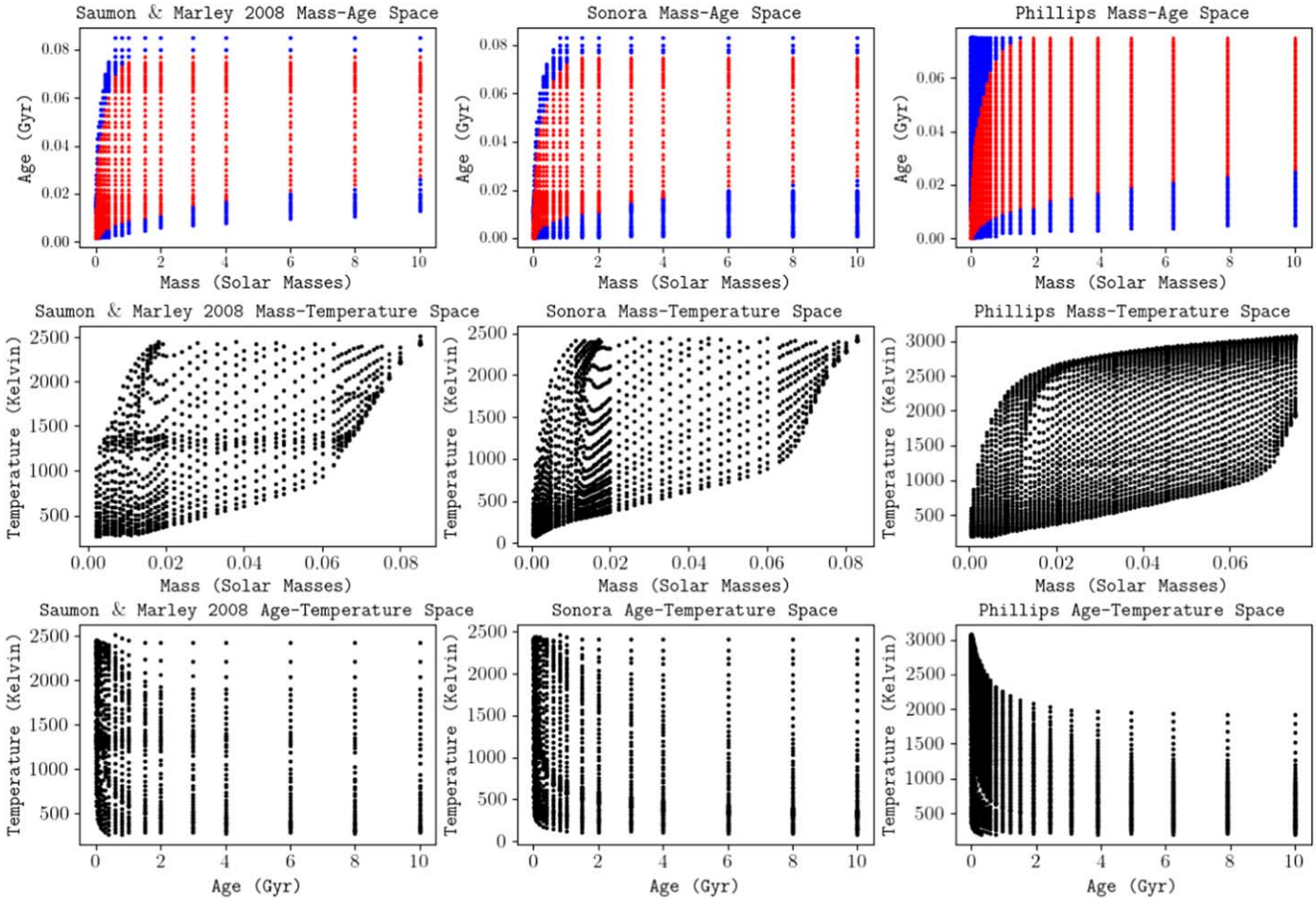

Figure 3. Plots of age vs. mass (top row), effective temperature vs. mass (middle row), and effective temperature vs. age (bottom row) for grid points in the three evolutionary model sets we consider: Saumon & Marley (2008), Sonora (Marley et al. 2021), and Phillips (Phillips et al. 2020). The red-colored triangular points in the top row are all evolutionary model points with a temperature between 450 K and 2100 K. In contrast, the top row's circular blue points are those that have temperature values outside of these bounds, namely, with temperatures <450 K or >2100 K.

(Section 5.1). From there, we propagate this population through the evolutionary model (Section 5.2), which provides a present-day value of the effective temperature for each object. All simulations were done in Python, using only fundamental libraries. The source code is available on our Github site.[12]

5.1. Choosing Mass Functions

We choose α values ranging from 0.3 to 0.8 in increments of 0.1, as they envelop the previous best α value of 0.6 (Kirkpatrick et al. 2019) on either side. Using the CDF^{-1} of our assumed mass distribution, we pull an object at random from the distribution to assign it a mass. This is done via a Monte Carlo draw from 0 to 1, and we perform 10^6 of these draws to build a population with statistical robustness. We repeat this procedure for each value of α, and for each value of α, we repeat the procedure for each of our three assumed low-mass cutoffs. In total, we build 18 simulated populations, each having masses for $n = 10^6$ objects. To be specific, the code samples the mass function again for each different combination of birthrate and evolutionary model, so in total, there are 162 simulated populations (six values of $\alpha \times$ three mass cutoffs $\times$ three birthrates $\times$ three evolutionary models).

[12] https://github.com/jgrigorian23/Brown-Dwarf-Simulation-Code

5.2. Constructing Mass–Age Brown Dwarf Populations

We similarly use the inverse transform method to pull random ages from each of our three assumed age distributions. This methodology allows for the creation of brown dwarf populations of arbitrary size whose mass distribution will converge to the shape of the transformed function as the sample size approaches a statistically significant value.

For each population, the *i*th element in each mass list and the *i*th element in the age list become the mass and age of the *i*th object in the simulated population.

5.3. Deriving Temperatures

For each object, we wish to find its current-day temperature using our assumed evolutionary model. However, given the discrete sampling of our evolutionary model grids, the simulated values of age and mass for our object are unlikely to have been included directly in the models. We therefore use bilinear interpolation to fill in the sample space between the model's reference points. Not all points in the mass–age domain can be mapped using bilinear interpolation. At the edges of the space sampled by each evolutionary model, there exist mass–age regions with points that cannot be enclosed within a rectangle of reference points. As shown in the left column of Figure 3, each evolutionary model has loci in which we cannot interpolate stellar temperatures.

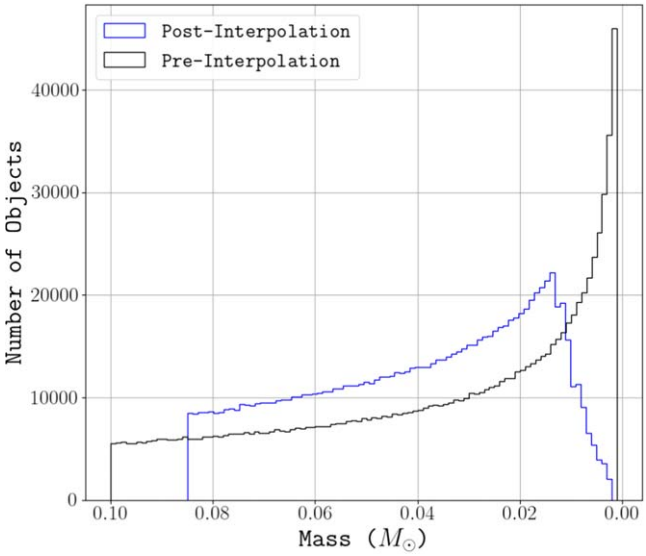

Figure 4. The mass distribution of the remaining simulated objects after evolutionary model interpolation for $\alpha = 0.5$ with the Saumon & Marley (2008) evolutionary model and a constant birthrate. The black graph is the original mass distribution with $\alpha = 0.5$, and the blue graph is the mass distribution of the remaining objects from the interpolation process.

In such cases, we simply disregard the star and assign to the star's temperature value the number -1 to indicate that a temperature could not be interpolated. The extent to which we lose objects during the interpolation depends on the (non)rectilinearity of the provided evolutionary sample set in mass–age space. Both the Sonora and Phillips models are fairly well sampled and do not drop many brown dwarf samples along the whole range of possible mass and age values. In contrast, the Saumon & Marley (2008) model drops the most objects of our three evolutionary models, especially those sample points that are either young and massive or old and light, as seen in the top left and bottom right of Figure 3. However, it should be noted that for the temperature range we consider for our fitting, namely, 450–2100 K, there are extremely few samples dropped due to a lack of rectilinear bounding reference points (see top row of Figure 3).

Although we state in Section 5.1 that we simulated $n = 10^6$ objects, in practice we simulated $n > 10^6$ objects and kept only the first 10^6 objects for which temperatures could be obtained via bilinear interpolation.

For our late-burst birthrate, we simulate brown dwarf subpopulations as explained at the end of Section 3.3. We shuffle these proportionally sampled constant and inside-out birthrate subpopulations and select the first 10^6 objects to create the late-burst birthrate.

The fact that the evolutionary model grids are not sampled over the entire mass and age space needed means that our final simulated populations contain small biases. See Figure 4 for an example of how our original mass distribution changes after interpolation.

6. Findings

6.1. Comparison to Empirical Data

We now shift focus to comparing our simulated populations to the empirical temperature distribution. We analyze our results in two steps. First, in Section 6.1.1, we describe our methods for comparing the simulated and observed temperature distributions to determine which low-mass function α value fits best. Then, in Section 6.1.2, we evaluate which mass cutoff leads to the best fit.

6.1.1. Temperature Distribution Fitting

For each simulated brown dwarf population, we consider only those objects with temperatures between 450 and 2100 K, as only that range is fully sampled. Many objects in the ranges 300–450 K and 2100–2400 K are dropped during the interpolation process; i.e., brown dwarfs falling in those ranges are underrepresented because of edges in the model grids.

We obtain our empirical data from Kirkpatrick et al.'s (2023) Table 17, as it provides a volume-limited sample of observed brown dwarfs within 20 pc of the Sun. To compare our models against the empirical data, we use the Levenberg–Marquardt algorithm as it is implemented in the IDL routine `mpfit` (Markwardt 2009). The Levenberg–Marquardt algorithm uniformly scales the simulated population's temperature distribution to find the best fit to the empirical distribution, necessary in our analysis as our distributions with millions of samples must be appropriately scaled down to be compared against the empirical distribution, which has only a few hundred data points total.

After many iterations, once the algorithm has optimized the best possible normalization between the two distributions, it returns the minimized residual, quantifying the agreement between the two. We rank our models by their residual value to find the best fit.

The five best fits for each of the three model suites are listed in Table 1. Note that the value of N is the Levenberg–Marquardt normalization constant, unique to each simulated population based on its optimal normalized fitting.

Since the empirical temperature distribution has a bump at the aforementioned L–T transition (1200–1350 K), any evolutionary model seeking to be accurate across the gamut of temperature must account for this. Only the Saumon & Marley (2008) model includes this, so its χ^2 values are naturally the lowest of the three model sets.

The χ^2 values of the five best-fitting populations displayed in Table 1 differ only by 0.19, and thus there are more similarly performing runs not shown in the table that must be considered when constraining the mass function. Figure 5 shows the α values of the brown dwarf simulations that fall within the first quartile. The conclusion from Kirkpatrick et al. (2021) that $\alpha = 0.6 \pm 0.1$ represents the best overall fit was based on a constant birthrate assumption, and as seen by Figure 5, this is reproduced in our study, since the distribution of well-performing simulations using a constant birthrate is centered around $\alpha = 0.6$ as well. Our study, which includes a wider set of birthrates, finds a preferred value of $\alpha = 0.5$, based on the peak seen in Figure 5. Among the models with $\alpha = 0.5$, the combination that yields the lowest reduced χ^2 is the one given by the Saumon & Marley (2008) atmospheric models, the late-burst birthrate, and a 0.001 $M_\odot$ cutoff. Therefore, we chose this combination as representative of the best overall fit (Figure 6). We note that Kirkpatrick et al. (2023) use a slightly different methodology (see their Section 7.1) and find a best fit of $\alpha = 0.6$ with the constant birthrate.

Table 1
The Five Best-fitting Simulations per Evolutionary Model Set

Model Set[a]	α	Birthrate	Low-mass Cutoff ($M_\odot$)	χ^2	N
(1)	(2)	(3)	(4)	(5)	(6)
SM08[b]	0.5	Late-burst	0.001	5.19	2427.32
SM08	0.6	Constant	0.01	5.19	2362.67
SM08	0.6	Constant	0.001	5.22	2478.73
SM08	0.6	Constant	0.005	5.24	2452.65
SM08	0.5	Constant	0.001	5.38	2416.51
Sonora	0.3	Constant	0.001	21.02	2687.96
Sonora	0.3	Constant	0.005	21.38	2422.72
Sonora	0.4	Constant	0.001	21.44	2859.21
Sonora	0.4	Constant	0.005	21.51	2501.77
Sonora	0.3	Constant	0.01	21.54	2183.54
Phillips	0.3	Constant	0.005	30.66	2270.93
Phillips	0.4	Constant	0.005	30.90	2357.76
Phillips	0.3	Constant	0.001	31.01	2342.49
Phillips	0.4	Constant	0.001	31.03	2458.24
Phillips	0.5	Constant	0.001	31.06	2591.57

Notes.
[a] SM08 = Saumon & Marley (2008); Phillips = Phillips et al. (2020); Sonora = Marley et al. (2021).
[b] This simulation serves as our choice of the best-fitting population.

6.1.2. Analysis of the Low-mass Cutoff

Our second round of analysis focuses on constraining the low-mass cutoff. We move our focus to the cold end of the temperature distribution, as the effects of the cutoff mass are most easily seen here.

The Saumon & Marley (2008) model grid has very sparse coverage of the lowest masses, so it is not very helpful in determining the low-mass cutoff. However, we can examine the low-mass cutoff using the best-fit mass and age distributions along the whole temperature range, $\alpha = 0.5$ and the constant birthrate, respectively (see left subplot of Figure 6), along with the best-sampled evolutionary model for low masses, the Phillips model, as this allows us to vary the low-mass cutoff specifically to view its impacts. We take the five best pairs of α and birthrate from the Saumon & Marley (2008) evolutionary model populations and find the corresponding populations that use the Phillips model instead. The results show that all of the five best α and birthrate models perform best with the 0.001 $M_\odot$ mass cutoff, and three of the five α and birthrate pairs have penultimate best fits with the 0.005 $M_\odot$ mass cutoff. This indicates that the low-mass cutoff is $\lesssim$0.005 $M_\odot$.

Our efforts in Section 6.1.1 reveal the combinations of mass function and birthrate that lead to the best-fitting temperature distributions. The best-performing mass shows a small skew toward the lower-mass cutoffs of 0.001 $M_\odot$ and 0.005 $M_\odot$, which correlates with previous result that the low-mass cutoff is at or below 0.005 $M_\odot$ in Kirkpatrick et al. (2019).

6.2. L/T Transition

A key feature of the Saumon & Marley (2008) evolutionary model is its incorporation of cloud formation at the L–T transition, in which L dwarfs cool into T dwarfs. This process is mainly limited to the temperature range from 1200 to 1350 K, and in this temperature bin, there is a noted increase of objects, forming a bump in the temperature distribution (Figure 6 and Figure 13 of Kirkpatrick et al. 2019). The exact physical conditions and processes that lead to this surplus of objects at 1200–1350 K are not yet fully understood, but one theory suggests that the dispersion of the cloud layers could be driven by a radiative cloud-induced variability (Tan & Showman 2019).

Figures 7 and 8 show the temperature distribution of our best-fit model colored by object age, showing an excess of young brown dwarfs at the L/T transition bin (1200–1350 K). This trend of younger brown dwarfs around the L/T transition is also visible in Figure 9, where we display the median age and its standard deviation per bin. These predictions suggest a pileup of young objects just prior to the L/T transition, indicating that the cooling time of a brown dwarf is significantly slowed in this region. Observational confirmation of this effect may be possible once we are able to collect a large field sample of brown dwarf age estimates or, perhaps more easily, measure the temperature distribution of L and T dwarfs belonging to young clusters and associations of known age.

6.3. Impacts of Changing α, Birthrate, Cutoff, or Model

The composition of each of our simulated populations depends heavily on our choice of mass function, birthrate, low-mass cutoff, and evolutionary model. In this section, we show the variation in the resulting temperature distribution when we hold all but one of these parameters constant.

The greatest change in the temperature distribution results from a change in the evolutionary model. Notably, simulations from the Saumon & Marley (2008) models possess a bump at the L/T transition, whereas those from both the Sonora and Phillips models do not.

As we vary the mass function α parameter, the shape of the temperature distribution also predictably varies (Figure 10). Flatter mass functions ($\alpha \sim 0.4$) lead to temperature distributions with relatively hotter objects, whereas steeper mass functions ($\alpha \sim 0.7$) lead to a greater abundance of cooler objects. Also, flatter mass functions imply a larger concentration of objects at the L/T transition with a lesser low-temperature peak (300–600 K), and vice versa for steeper mass functions. It should be noted that other differences are marginal everywhere except the low-temperature peak, where the difference between the $\alpha = 0.3$ and $\alpha = 0.8$ distributions is pronounced. Fundamentally, increasing the mass function's steepness serves to skew the resulting temperature distribution toward the cooler end of the temperature regime.

Differences in birthrate functions have already been shown to affect the resulting temperature distribution only marginally (Burgasser 2004). Our findings corroborate this (Figure 11).

Nonetheless, the inside-out age function, for example, allows for a flatter mass function to fit the empirical temperature distribution. The $\alpha = 0.6$ value taken as the ideal mass function steepness in Kirkpatrick et al. (2019) assumed a constant birthrate, and our findings in Table 1 replicate that while also showing that a combination of $\alpha = 0.4$ or $\alpha = 0.5$ paired with an inside-out birthrate also fit the empirical data quite well. This is because the declining birthrate represented by the inside-out function paired with a less steep (lower α) mass function can create as many present-day late T and Y dwarfs as a constant birthrate paired with a steeper mass function.

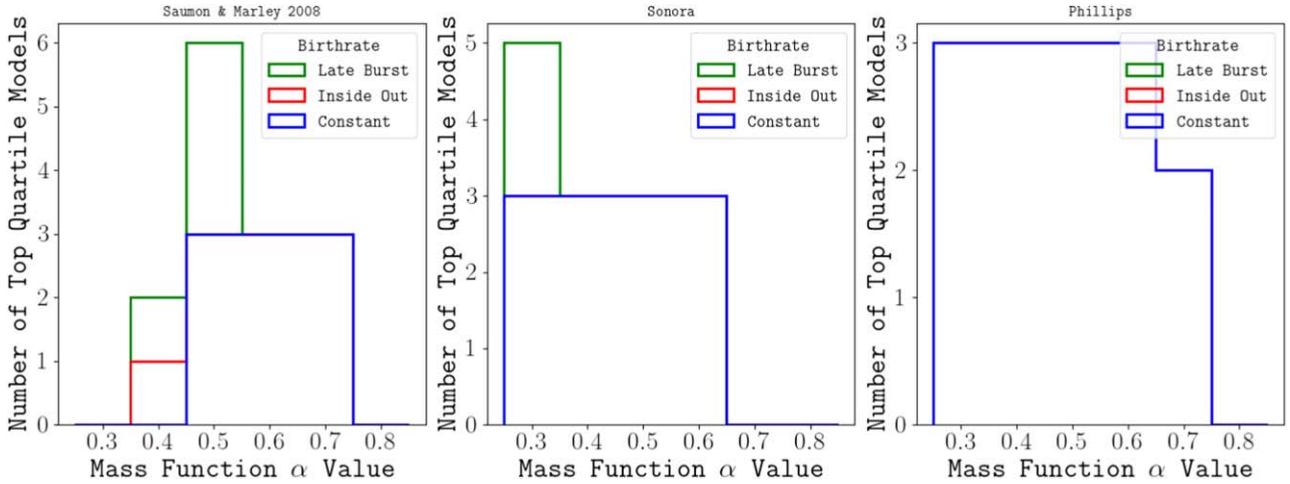

Figure 5. The first quartile of the best-fitting brown dwarf populations colored by their birthrate for each of our evolutionary models.

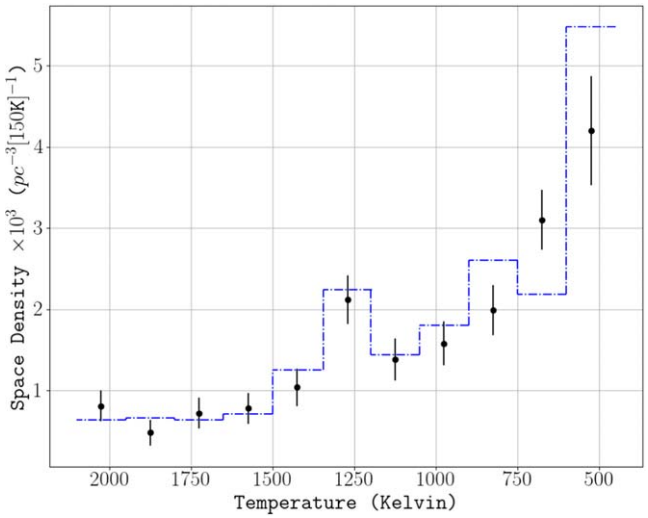

Figure 6. Our preferred "best-fit" simulation (blue dashed line)—$\alpha = 0.5$, late-burst birthrate, low-mass cutoff of 0.001 $M_{\odot}$, and Saumon & Marley (2008) evolutionary model grid—compared to the observed space density of brown dwarfs within the 20 pc census (black points with uncertainties) from Kirkpatrick et al. (2023).

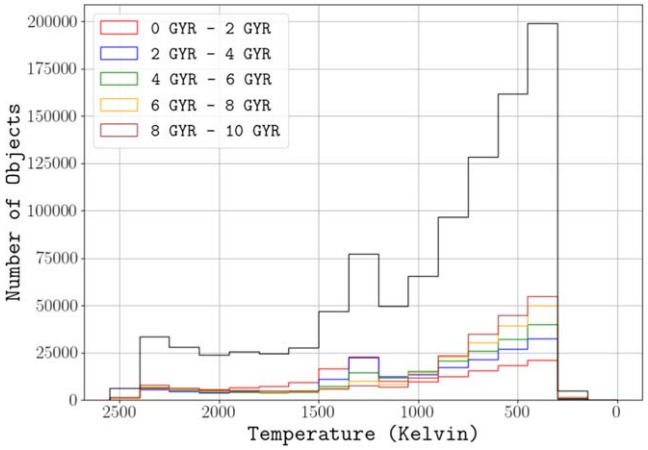

Figure 7. The temperature distribution of our best-fit simulation (black line; $\alpha = 0.5$, late-burst birthrate, low-mass cutoff of 0.001 $M_{\odot}$, and Saumon & Marley 2008 evolutionary model) decomposed into age regimes (colored lines).

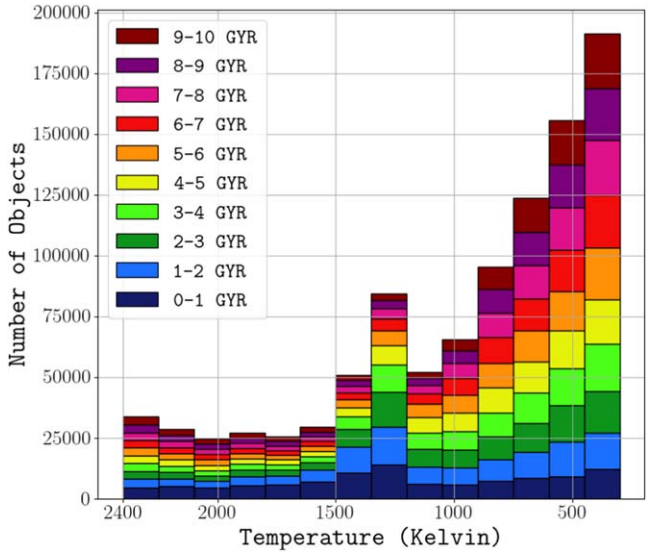

Figure 8. The temperature distribution of our best-fit simulation ($\alpha = 0.5$, late-burst birthrate, low-mass cutoff of 0.001 $M_{\odot}$, and the Saumon & Marley 2008 evolutionary models) color coded by the age of each object.

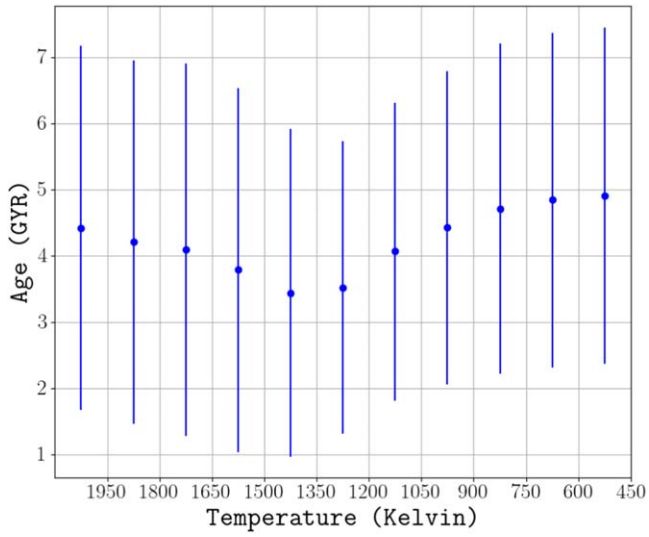

Figure 9. The median age and standard deviation in each temperature bin from Figure 8.

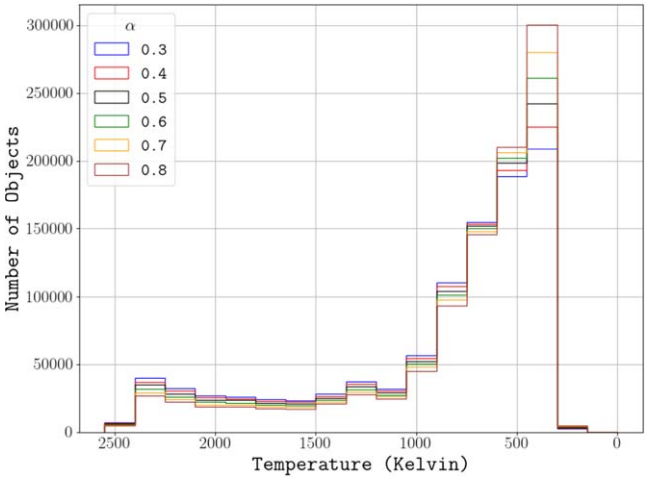

Figure 10. Temperature distributions for simulated brown dwarf populations with a varying mass function α parameter ($\alpha \in \{0.3, 0.4, 0.5, 0.6, 0.8\}$). The birthrate is the constant birthrate with a low-mass cutoff of 0.001 $M_{\odot}$ and the Saumon & Marley (2008) evolutionary model.

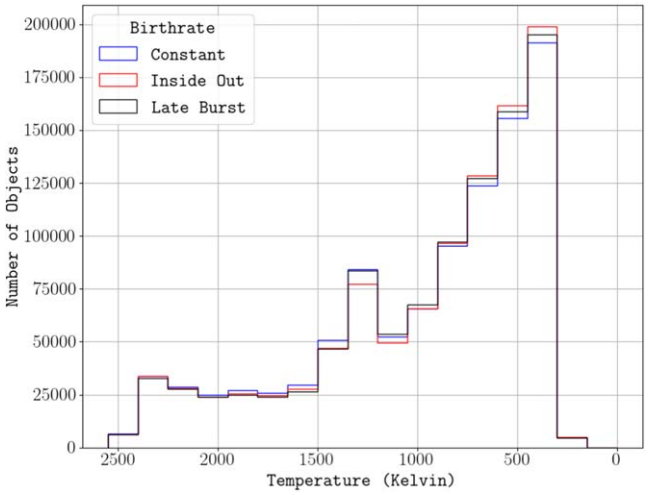

Figure 11. Temperature distributions for simulated brown dwarf populations with a varying age function parameter. The low-mass cutoff is 0.001 $M_{\odot}$ with an α of 0.5 and the Saumon & Marley (2008) evolutionary model. The three assumed birthrates are constant (blue), inside-out (red), and late-burst (black) from Section 3.

The mass cutoff also does not in any significant way affect the shape of the simulated temperature distribution except at the coldest temperatures (Figure 12).

7. Conclusions

Our study presents an updated approach to determine the mass function through brown dwarf population simulations. We pose several power-law mass functions and combine them with three sample birthrates to create a suite of simulated brown dwarf populations whose temperature distributions we compare to the empirical temperature distribution from Kirkpatrick et al. (2021). Our results indicate a best fit of $\alpha = 0.5$ for a birthrate from Johnson et al. (2021; their so-called "inside-out" function) that has been steadily declining over the lifetime of the Milky Way, or $\alpha = 0.6$ for a constant birthrate, which agrees with a previous study done using the same methodology (Kirkpatrick et al. 2019). Our study finds that the low-mass cutoff is $\lesssim 0.005\ M_{\odot}$ by

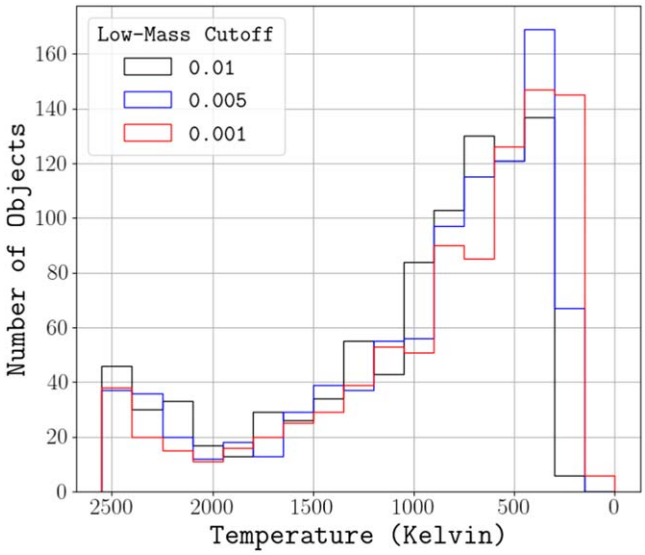

Figure 12. Temperature distributions for simulated brown dwarf populations with a varying low-mass cutoff parameter (mass cutoffs: 0.01 $M_{\odot}$, 0.005 $M_{\odot}$, 0.001 $M_{\odot}$). Mass function α: 0.5; birthrate: inside-out; evolutionary model: Phillips (Phillips et al. 2020).

examining the best-performing mass cutoffs. However, tighter error bars on the space density of Y dwarfs within 20 pc would place tighter constraints on α while also increasing confidence in the low-mass cutoff and, if a plethora of even colder Y dwarfs is found, push the cutoff value even lower.

All of the code we used to simulate our populations was written in Python and is publicly available on Zenodo[13] (Raghu & Grigorian 2024). Our formalism allows for brown dwarf population simulations for a given mass function, age function, evolutionary model, and low-mass cutoff. One such use case of this code is outlined in the Appendix, where we modify our birthrate to only include stars with ages 8–10 Gyr. Applications like these are possible because of the flexible nature of our code base, as it allows for great customization of parameters such as mass function and age function. Methodology such as ours is a step toward piecing together the properties of brown dwarfs that are harder to access through direct observation, as one can imagine using evolutionary models with absolute bolometric luminosity measurements instead of empirically derived effective temperatures, as we have done here. Ultimately, it is further observed brown dwarf data that are sorely needed to stimulate a more precise theory.

Acknowledgments

Support for this work was provided by NASA through Backyard Worlds grant 2017-ADAP17-0067 and by NASA through a grant for James Webb Space Telescope program #2302 from the Space Telescope Science Institute, which is operated by the Association of Universities for Research in Astronomy, Inc., under NASA contract NAS 5-03127.

Appendix
Present-day Temperature Distribution for Old Brown Dwarfs

One interesting application of the simulation framework we have built is our ability to tweak the input parameters to explore

[13] doi:10.5281/zenodo.11479693

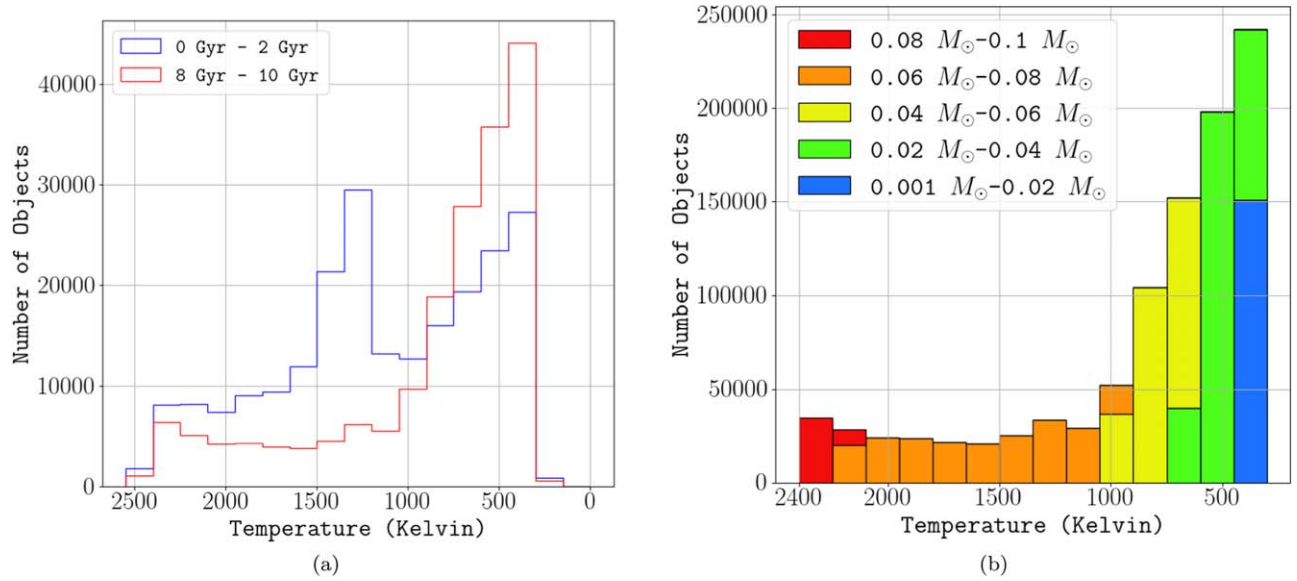

Figure A1. (a) The temperature distribution for old brown dwarfs with ages 8–10 Gyr with varying mass cutoffs of 0.01 $M_\odot$, 0.005 $M_\odot$, or 0.001 $M_\odot$. (b) The temperature distribution of objects with ages of 8–10 Gyr further color coded by mass.

other physical scenarios. In this section, we examine the predicted present-day temperature distribution of old stars (8–10 Gyr). We choose $\alpha = 0.5$, a low-mass cutoff of 0.001 $M_\odot$, and the Saumon & Marley (2008) evolutionary models. For simplicity, we choose our age function as simply a constant birthrate ranging from 8 to 10 Gyr. With these parameters, we build a temperature distribution via our publicly available code.

Figure A1(a) shows this temperature distribution, ultimately revealing how old stars have thermally evolved over time. As discussed in Section 6.2, the L/T transition bump in the temperature distribution consists mainly of younger objects, so it is no surprise that the temperature distribution of older objects shown here lacks such a bump. Figure A1(a) shows the change in the temperature distribution for young (0–2 Gyr) brown dwarfs and old (8–10 Gyr) brown dwarfs. Figure A1(b) agrees with the standard knowledge on low-mass brown dwarfs, as they are heavily skewed toward colder temperature bins.

ORCID iDs

Yadukrishna Raghu https://orcid.org/0000-0001-9778-7054
J. Davy Kirkpatrick https://orcid.org/0000-0003-4269-260X
Federico Marocco https://orcid.org/0000-0001-7519-1700
Christopher R. Gelino https://orcid.org/0000-0001-5072-4574
Daniella C. Bardalez Gagliuffi https://orcid.org/0000-0001-8170-7072
Jacqueline K. Faherty https://orcid.org/0000-0001-6251-0573
Steven D. Schurr https://orcid.org/0000-0003-1785-5550
Adam C. Schneider https://orcid.org/0000-0002-6294-5937
Aaron M. Meisner https://orcid.org/0000-0002-1125-7384
Marc J. Kuchner https://orcid.org/0000-0002-2387-5489
Hunter Brooks https://orcid.org/0000-0002-5253-0383
Jake Grigorian https://orcid.org/0000-0002-2466-865X

References

Bate, M. R., & Bonnell, I. A. 2005, MNRAS, 356, 1201
Bird, J. C., Kazantzidis, S., Weinberg, D. H., et al. 2013, ApJ, 773, 43
Burgasser, A. J. 2004, ApJS, 155, 191
Burrows, A., Sudarsky, D., & Hubeny, I. 2006, ApJ, 640, 1063
Carroll, B. W., & Ostlie, D. A. 1996, in An Introduction to Modern Astrophysics, Benjamin Cummings, ed. B. W. Carroll & D. A. Ostlie (New York: Benjamin-Cummings), 1996
Chabrier, G. 2001, ApJ, 554, 1274
Chabrier, G. 2003a, PASP, 115, 763
Chabrier, G. 2003b, ApJL, 586, L133
Chabrier, G., & Lenoble, R. 2023, ApJL, 944, L33
Cushing, M. C., Kirkpatrick, J. D., Gelino, C. R., et al. 2014, AJ, 147, 113
Dominik, M., & Sahu, K. C. 2000, ApJ, 534, 213
Faherty, J. K., Riedel, A. R., Cruz, K. L., et al. 2016, ApJS, 225, 10
Faherty, J. K., Tinney, C. G., Skemer, A., et al. 2014, ApJL, 793, L16
Gagné, J., Faherty, J. K., Burgasser, A. J., et al. 2017, ApJL, 841, L1
Hayashi, C., & Nakano, T. 1963, PThPh, 30, 460
Helmi, A. 2020, ARA&A, 58, 205
Johnson, J. W., Weinberg, D. H., Vincenzo, F., et al. 2021, MNRAS, 508, 4484
Kapteyn, J. C. 1903, Skew Frequency Curves in Biology and Statistics (Groningen: Noordhoff), https://ia902809.us.archive.org/14/items/skewfrequencycur00kaptuoft/skewfrequencycur00kaptuoft.pdf
Kirkpatrick, J. D., Gelino, C. R., Faherty, J. K., et al. 2021, ApJS, 253, 7
Kirkpatrick, J. D., Marocco, F., Gelino, C. R., et al. 2024, ApJS, 271, 55
Kirkpatrick, J. D., Martin, E. C., Smart, R. L., et al. 2019, ApJS, 240, 19
Kroupa, P., Weidner, C., Pflamm-Altenburg, J., et al. 2013, in Planets, Stars and Stellar Systems. Volume 5: Galactic Structure and Stellar Populations, ed. T. D. Oswalt & G. Gilmore (Berlin: Springer), 115
Kumar, S. S. 1963, ApJ, 137, 1121
Leggett, S. K., Tremblin, P., Esplin, T. L., et al. 2017, ApJ, 842, 118
Liu, M. C., Dupuy, T. J., & Allers, K. N. 2016, ApJ, 833, 96
Markwardt, C. B. 2009, in ASP Conf. Ser. 411, Astronomical Data Analysis Software and Systems XVIII, ed. D. A. Bohlender, D. Durand, & P. Dowler (San Francisco, CA: ASP), 251
Marley, M. S., Saumon, D., Visscher, C., et al. 2021, ApJ, 920, 85
Miller, G. E., & Scalo, J. M. 1979, ApJS, 41, 513
Nakajima, T., Oppenheimer, B. R., Kulkarni, S. R., et al. 1995, Natur, 378, 463
Nonino, M., Glazebrook, K., Burgasser, A. J., et al. 2023, ApJL, 942, L29
Oppenheimer, B. R., Kulkarni, S. R., Matthews, K., et al. 1995, Sci, 270, 1478
Phillips, M. W., Tremblin, P., Baraffe, I., et al. 2020, A&A, 637, A38
Raghu, Y., & Grigorian, J. 2024, jgrigorian23/Brown-Dwarf-Simulation-Code: Brown Dwarf Simulation Code Official Public Release, v1.0, Zenodo, doi:10.5281/zenodo.11479712
Ruiz-Lara, T., Gallart, C., Bernard, E. J., et al. 2020, NatAs, 4, 965
Salpeter, E. E. 1955, ApJ, 121, 161
Saumon, D., & Marley, M. S. 2008, ApJ, 689, 1327
Spiegel, D. S., Burrows, A., & Milsom, J. A. 2011, ApJ, 727, 57
Tan, X., & Showman, A. P. 2019, ApJ, 874, 111
Werner, M. W., Roellig, T. L., Low, F. J., et al. 2004, ApJS, 154, 1
Wright, E. L., Eisenhardt, P. R. M., Mainzer, A. K., et al. 2010, AJ, 140, 1868